



Influence of La additions on solidification and microstructure in the as-cast state of the aluminium alloy EN AW-7175

Tilen Balaško¹ · Maja Vončina¹ · Aleš Nagode¹ · Jožef Medved¹

Received: 12 September 2023 / Accepted: 21 April 2024
© The Author(s) 2024

Abstract

The high-strength aluminium alloys of the 7xxx series, which belong to the Al–Zn–Mg–Cu system, are known for their exceptional properties and are often used for applications where strength, fatigue resistance, stress corrosion resistance and wear resistance are required. The alloy EN AW-7175 requires an understanding of the precipitation process during solidification and cooling, where different phases are formed depending on the Zn/Mg ratio and cooling rate. Microstructural defects in the as-cast state affect the mechanical properties, prompting the investigation of La additions to refine the microstructure and improve the mechanical properties. In this study, the influence of La additions on the solidification and microstructure of the alloy EN AW-7175 in the as-cast state is investigated. Thermodynamic calculations, DSC and SEM analyses were performed. Samples with La additions (0.05–0.17 mass%) were compared with a reference sample (0 mass% La). La additives have only a minimal effect on the liquidus temperature and show minor differences in the solidus temperature in equilibrium calculations. The solidification interval decreases slightly compared to the reference sample, which is consistent with the Scheil simulations. The DSC results show reduced liquidus and solidus temperatures, while the solidification interval remains largely unchanged by the addition of La. The addition of La alongside Al₁₃Fe₄, Mg₂Si and the eutectic $\alpha(\text{Al}) + \sigma[\text{Mg}(\text{Zn}, \text{Cu}, \text{Al})_2]$ leads to the formation of two new La-based phases: Al₂₀Cr₂La and LaSi₂. Al₂₀Cr₂La modifies the Al₄₅Cr₇ phase and solidifies first, while LaSi₂ modifies Mg₂Si. As the La content increases, the Mg₂Si content decreases until it completely disappears at a La content of more than 0.1 mass%. On the contrary, according to the literature, the grain size increases somewhat with a higher La content.

Keywords EN AW-7175 · Solidification · Microstructure · CALPHAD · DSC

Introduction

The high-strength 7xxx series are aluminium alloys from the Al–Zn–Mg–Cu alloy system. They are heat treatable alloys characterised by high-strength, limited fatigue strength, stress corrosion resistance and excellent wear resistance [1–16]. They are widely used as structural materials in aerospace, rail, automotive and other industries due to their high-strength-to-mass ratio achieved by heat treatment [1, 2, 5, 6, 9–13, 15–17]. EN AW-7175 alloy is one of the newer variants from the Al–Zn–Mg–Cu alloy system based on the alloy EN AW-7075 [8]. The precipitations during solidification/cooling of the 7xxx alloy system are important and complex.

Studies by numerous researchers [1–10, 12–16, 18–21] have identified phases that precipitate (in addition to $\alpha\text{-Al}$) during the solidification/cooling process of the Al–Zn–Mg–Cu alloy system. They are shown in Table 1. In these studies, it was also shown that the stoichiometry of the M/ η , S, T, V, and Z phases varies greatly and depends on the Zn/Mg ratio and the cooling rates, which is why the composition of the phases is usually given with minimum and maximum values. Previous studies [1, 8, 15] also indicated that when the Zn/Mg ratio is below 2.2, the main strengthening phase is T, while when the ratio is above 2.2, the main strengthening phase is η/M . Lim et al. [8] investigated the Zn/Mg ratio in the alloy EN AW-7175 and found that a lower (Cu + Mg) content and a higher Zn/Mg ratio (3.0) compared to a higher (Cu + Mg) content and a lower Zn/Mg ratio (2.0) resulted in a lower solvus of the S phase and thus a coarse S phase.

In general, 7xxx series alloys do not provide their best as-cast mechanical properties and performance due to

✉ Tilen Balaško
tilen.balasko@ntf.uni-lj.si

¹ Faculty of Natural Sciences and Engineering, University of Ljubljana, Aškerčeva Cesta 12, 1000 Ljubljana, Slovenia

Table 1 List of phases precipitated during the solidification and cooling process of the Al-Zn-Cu-Mg alloy system

Phases	Formula	Phases	Formula
Metastable Al ₃ Zr	Al ₃ Zr	η/M	MgZn ₂
Mg ₂ Si	Mg ₂ Si	S	Al ₂ CuMg
Al ₇ Cr	Al ₇ Cr	T	Al ₂ Mg ₃ Zn ₃ , Mg ₃₂ (Al, Cu, Zn) ₄₉ , AlCuMgZn
Al ₃ Fe	Al ₃ Fe	V/Z	Mg ₂ Zn ₁₁ + Al ₅ Cu ₆ Mg ₂
Al ₁₃ Fe ₄	Al ₁₃ Fe ₄	σ (T + η/M)	Mg(Zn, Cu, Al) ₂
Al ₇ Cu ₂ Fe	Al ₇ Cu ₂ Fe	θ	Al ₂ Cu

inherent microstructural deficiencies such as coarse intermetallic phases, micro and macro segregation, coarse grains, and hot cracking [9, 17]. Hot tearing could be overcome during solidification by two methods: Refining the secondary dendrite arm spacing (SDAS) of the primary α-Al phase and/or by changing the morphology of this phase to a non-dendritic phase [9]. This is one of the reasons why the addition of La has been investigated, as previous studies [22–25] have reported that it promotes the refinement of the SDAS of the primary α-Al phase/grains. And it is important to first understand the effects of La additions on the solidification process and as-cast phase evolution to successfully achieve optimal temperatures for further heat treatment to achieve the desired mechanical properties. Previous studies [22–30] have also shown that the addition of La increases mechanical properties and corrosion resistance.

Based on the above findings, we decided to investigate the influence of La additions on the solidification and phase evolution of the alloy EN AW-7175 in the as-cast state. Thermodynamic calculations based on the CALPHAD method were carried out, using equilibrium calculations and solidification simulations according to Scheil. In addition, DSC (differential scanning calorimetry) analyses were carried out to evaluate the influence of the La additives on the solidification process, and microstructural analyses were carried out using SEM (scanning electron microscopy) to evaluate the microstructural components of the investigated as-cast samples and the influence of the La additives on the phase evolution. The alloy EN AW-7175 (sample 0) served as a reference and the other samples had

Table 3 Amount of Cu+Mg, Zn+Mg+Cu in mass% and ratio Zn/Mg calculated from mass%

Sample	Cu+Mg	Zn+Mg+Cu	Zn/Mg
0	3.83	9.34	2.42
1	3.75	9.22	2.42
2	3.83	9.41	2.45
3	3.78	9.31	2.45
4	3.80	9.29	2.39

elevated La additions (0.05, 0.1, 0.14 and 0.17 mass%—samples 1, 2, 3 and 4 respectively).

Experimental work

Since the aim of the study was to investigate the solidification and phase evolution of the alloy EN AW-7175 in the as-cast condition, DSC analyses and metallography were carried out after the preparation of the alloys. CALPHAD calculations were also carried out to evaluate the thermodynamically stable phases of the samples studied and the influence of La addition on phase evolution.

Materials

For each batch, 500 g of a commercial EN AW-7175 alloy was melted. The alloys were produced in an electric resistance furnace with a graphite crucible covered with a calcium silicate (Ca₂O₄Si) to prevent heat loss and ensure stability of the melt. The melt was heated to 750 °C, which was also the pouring temperature for each batch. After the addition of La (99.99 mass%), the melt was skimmed off and poured into permanent moulds. The temperature of the melt was controlled with a K-type thermocouple. As the aim was to ensure that the metallurgical process parameters were the same for each batch, sample 0 (reference) was also remelted and cast.

The chemical composition (Table 2) was measured with OES ARL iSpark 8860.

Since the amount of Cu, Mg and Zn and the ratio Zn/Mg are important, they were also calculated and are shown in Table 3. The amounts and the ratio are almost the same for

Table 2 Chemical composition of the investigated alloys in mass%

Sample	Si	Fe	Cu	Mn	Mg	Cr	Ni	Zn	Ti	V	La	Al
0	0.08	0.12	1.55	0.03	2.28	0.20	0.01	5.51	0.03	0.01	0.0	Bal.
1	0.07	0.12	1.49	0.02	2.26	0.20	0.01	5.47	0.03	0.01	0.05	Bal.
2	0.08	0.13	1.55	0.04	2.28	0.20	0.01	5.58	0.03	0.01	0.10	Bal.
3	0.08	0.13	1.52	0.04	2.26	0.21	0.01	5.53	0.03	0.01	0.14	Bal.
4	0.07	0.11	1.50	0.02	2.30	0.20	0.01	5.49	0.03	0.01	0.17	Bal.

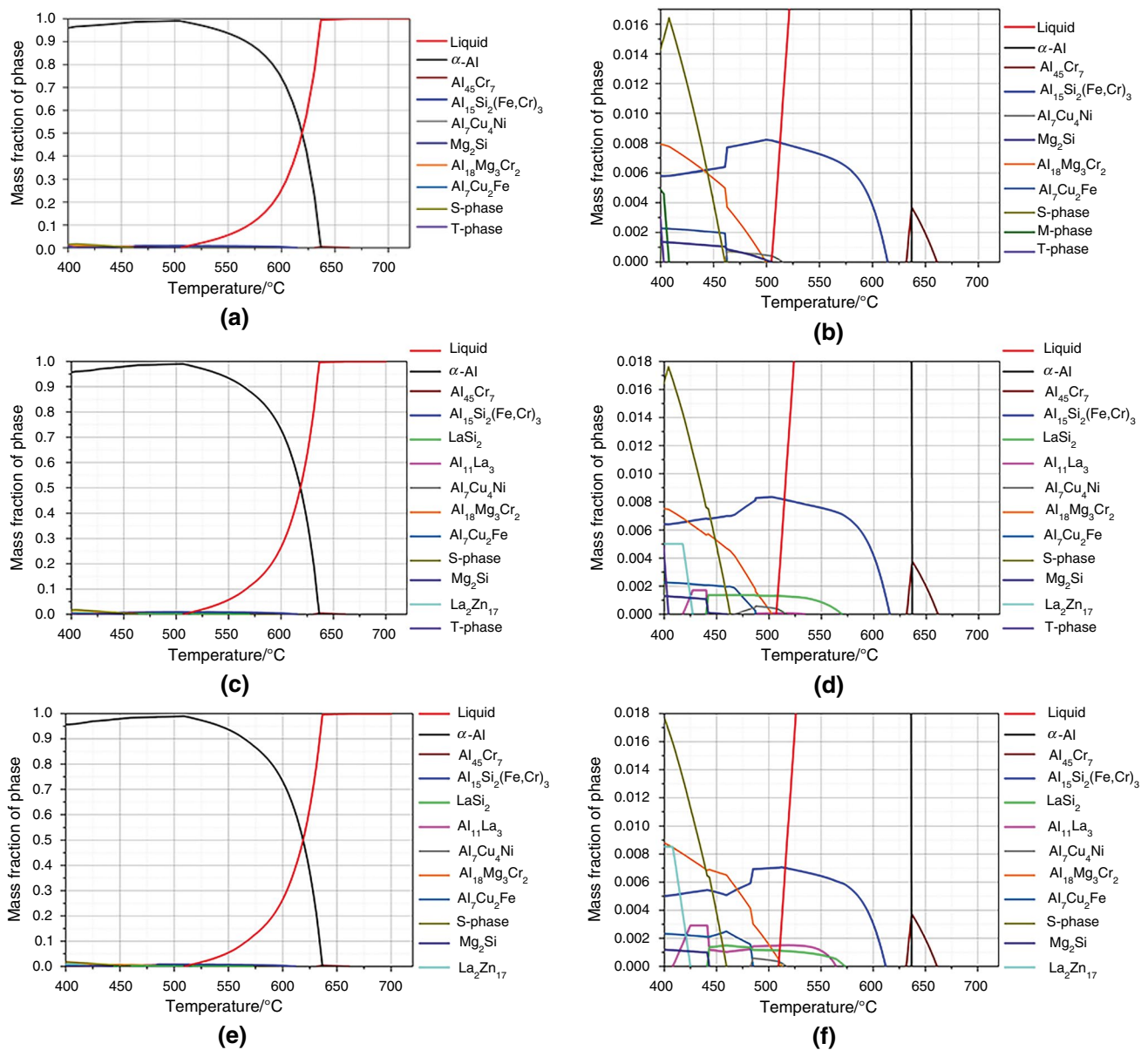


Fig. 1 Mass fraction of all thermodynamically stable equilibrium phases as a function of temperature for sample 0 (a) and (b—magnification of a), sample 2 (c) and (d—magnification of c) and sample 4 (e) and (f—magnification of e)

all samples examined. Since the Zn/Mg ratio is above 2.2, according to the literature [1, 8, 15] the main strengthening phase should be η/M .

Calculation of phase diagrams (CALPHAD)

The commercial Thermo-Calc software version 2023a was used for the CALPHAD modelling. The Thermo-Calc Software TCAL8 Aluminium-based Alloys database was selected from which the thermodynamic data for the

calculations were obtained. A one axis type of calculation was chosen for the equilibrium calculations, from which plots were obtained showing the amount of thermodynamically stable phases in the alloys studied. Since, solidification and phase evolution were studied in the as-cast state, the determination of solidification under non-equilibrium conditions was calculated using the classical model of Scheil [31, 32] (Scheil-Gulliver solidification simulation). The model assumes that the diffusion of all elements in the liquid phase

Table 4 Liquidus temperatures of the equilibrium phases in the temperature range between 400 °C and 720 °C

Phase	Liquidus temperature/°C				
	0	1	2	3	4
Al ₄₅ Cr ₇	664	663	664	666	664
α-Al	637	637	637	637	637
Al ₁₅ Si ₂ (Fe,Cr) ₃	614	614	615	616	612
LaSi ₂	–	562	570	573	573
Al ₇ Cu ₄ Ni	515	517	516	517	517
Mg ₂ Si	505	471	460	442	443
Al ₁₈ Mg ₃ Cr	500	504	503	508	513
Al ₇ Cu ₂ Fe	463	462	488	484	485
S-Phase	461	459	463	460	460
Al ₁₁ La ₃	–	441	442	557	564
La ₂ Zn ₁₇	–	424	427	426	425
T-Phase	408	405	404	401	–

Table 5 Mass fraction of the thermodynamically stable equilibrium phases at 400 °C in all investigated samples

Phase	Mass fraction of the phase at 400 °C				
	0	1	2	3	4
Al ₄₅ Cr ₇	–	–	–	–	–
α-Al	0.960	0.960	0.957	0.957	0.956
Al ₁₅ Si ₂ (Fe,Cr) ₃	0.006	0.006	0.006	0.006	0.005
LaSi ₂	–	–	–	–	–
Al ₇ Cu ₄ Ni	–	–	–	–	–
Mg ₂ Si	0.001	0.001	0.001	0.001	0.001
Al ₁₈ Mg ₃ Cr	0.008	0.008	0.008	0.008	0.009
Al ₇ Cu ₂ Fe	0.002	0.002	0.002	0.002	0.002
S-Phase	0.015	0.015	0.017	0.018	0.018
Al ₁₁ La ₃ *	–	–	–	–	–
La ₂ Zn ₁₇	–	0.003	0.005	0.007	0.009
T-Phase	0.008	0.005	0.004	0.001	–

is infinitely fast (complete mixing in the liquid), that there is no diffusion in the solid (the diffusion of all elements in the solid phases is zero) and that the interface between the liquid and the solid is in complete thermodynamic equilibrium. It is a well-known model and is often used in studies [33–37] on the solidification of metals and alloys.

Differential scanning calorimetry (DSC)

For the DSC analysis, samples with dimensions of approximately 4 × 3.5 × 1.5 mm (± 0.2 mm) and a mass between 30 and 50 mg were prepared from the produced alloys. The solidification process was investigated with the NETZSCH DSC 404 F3 Pegasus device. The samples were heated to 720 °C at a heating rate of 10 K min⁻¹ and cooled to room

temperature at a cooling rate of 10 K min⁻¹, with the furnace under Ar protective atmosphere throughout the analysis. Empty DSC crucibles made of Al₂O₃ were used as reference. Only the cooling curves were used for further analysis, as solidification was investigated. DSC analysis was used to determine the characteristic temperatures of the solidification process, such as the liquidus, solidus and phase precipitation/solidification start temperatures. All peaks on the DSC cooling curves were determined with NETZSCH Proteus® software using the tangent method. To ensure that we determined the exact temperatures for shallower sections, in our case for the Al₁₃Fe₄ and Mg₂Si/LaSi₂ phases (as the amount of these phases was small), the first derivative was calculated and the inflexion points on the first derivative curve were used to determine the characteristic temperatures for the mentioned phases, even if they are visible on the DSC cooling curve. But to be on the safe side, we check them again with the derivative. DSC analysis has been shown to provide very accurate results when investigating the solidification process of metals and alloys, as reported in previous studies [38–41].

Metallography

The samples for metallography were ground and polished. Metallographic analysis was performed using the ThermoFisher Scientific Quattro S FEG-SEM (field emission gun scanning electron microscopy). The latter was used for phase analysis with the analyser EDS (energy-dispersive X-ray spectroscopy) Ultim® Max Oxford Instruments, where element mapping, chemical composition of the phases and line scanning were performed.

Results and discussion

The results of the CALPHAD and DSC analysis shown are in the temperature range between 400 and 720 °C, as the solidification process and phase development were investigated in the cast state. Sample 0 is used as a reference sample without La addition.

CALPHAD analysis

Based on the results of the calculated thermodynamically stable equilibrium phases for the samples studied, there were minor differences, we have only drawn diagrams for samples 0, 2 and 4 (Fig. 1) as they are the most representative. All results concerning solidus, liquidus and precipitation temperatures are shown in Table 4. In addition, the mass fractions of the phases stable at 400 °C in the samples studied (Table 5) have been shown.

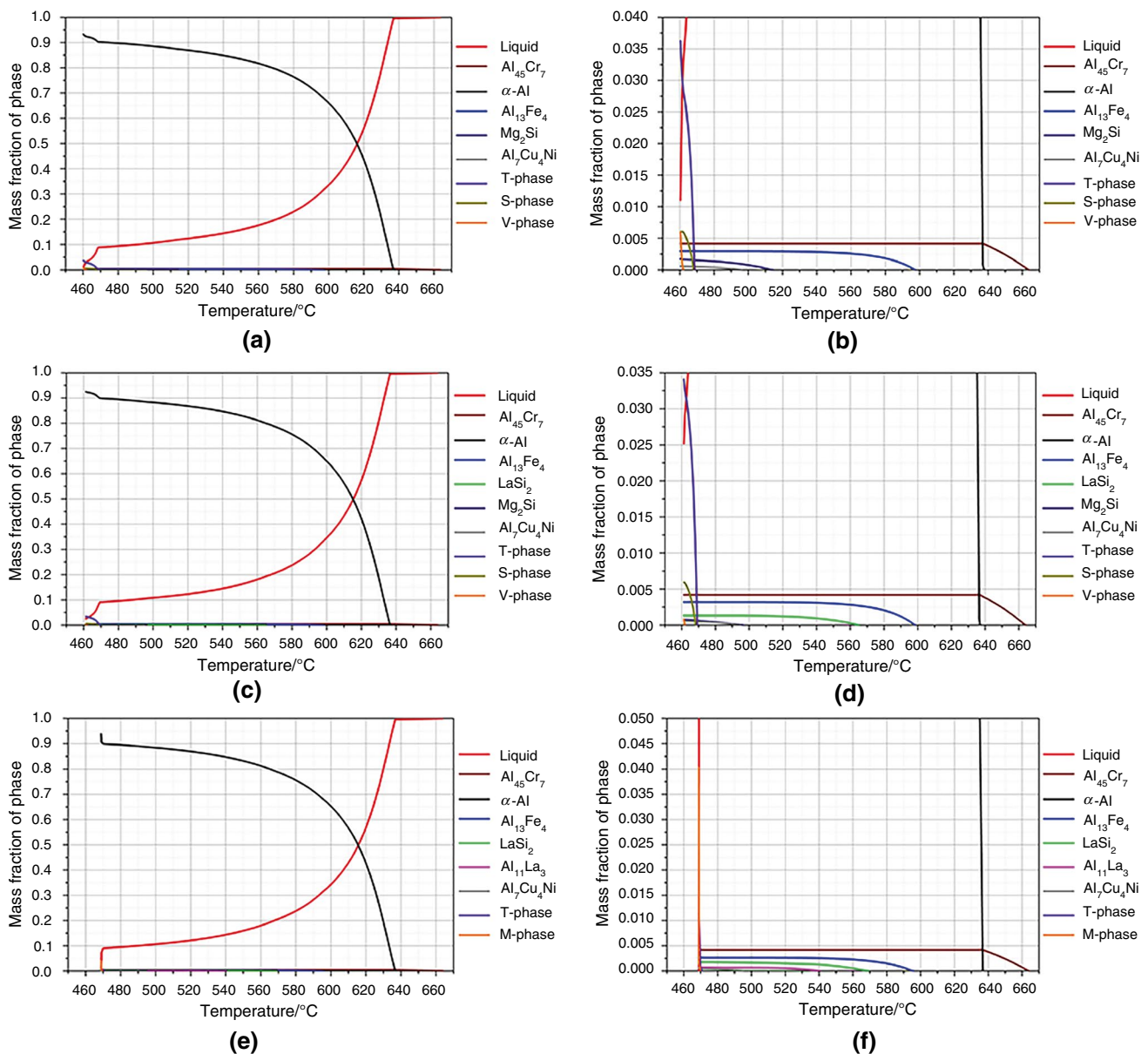


Fig. 2 Mass fraction of the phases solidified during the Scheil solidification calculation sample 0 (**a**) and (**b**—magnification of a), sample 2 (**c**) and (**d**—magnification of c) and sample 4 (**e**) and (**f**—magnification of e)

Since the effect of La addition on solidification was investigated, we first looked at the liquidus and solidus temperatures. For sample 0 the liquidus temperature is 663.6 °C, for sample 1 663.4 °C, for sample 2 663.8 °C, for sample 3 665.8 °C and for sample 4 663.8 °C. On the other hand, the solidus temperature for sample 0 is 504.5 °C, for sample 1 510.8 °C, for sample 2 506.7 °C, for sample 3 509.0 °C and for sample 4 509.2 °C. As can be seen from the calculated results, there are minor changes in the liquidus and solidus temperatures, with the former remaining almost unchanged and the latter increasing slightly compared to reference sample 0 (6.3, 2.2, 4.5 and 4.7 °C for samples 1, 2,

3 and 4, respectively). Meanwhile, the solidification interval ($T_L - T_S$) is slightly reduced by the addition of La compared to reference sample 0 (the maximum difference is 6.5 °C in the case of sample 1, the others are smaller), but no significant differences can be observed.

In the following table (Table 4), the liquidus temperatures of the thermodynamically stable equilibrium phases are compiled for all samples investigated. According to the calculations, three new phases are formed by the addition of La to the alloy EN AW-7175: LaSi_2 , $\text{Al}_{11}\text{La}_3$ and $\text{La}_2\text{Zn}_{11}$. Compared to the reference sample (0), the addition

Table 6 Liquidus temperatures of the phases in the Scheil solidification simulation for the investigated samples

Phase	Liquidus temperatures/°C				
	0	1	2	3	4
Al ₄₅ Cr ₇	663.6	663.4	663.8	665.8	663.8
α _{Al}	636.9	637.2	636.5	636.7	636.7
Al ₁₃ Fe ₄	597.3	597.5	598.3	598.4	595.1
LaSi ₂	–	554.5	565.0	569.3	568.4
Mg ₂ Si	513.5	503.0	496.1	–	–
Al ₇ Cu ₄ Ni	495.9	495.3	495.0	495.2	494.8
Al ₁₁ La ₃	–	–	–	–	540.0
T-Phase	468.6	469.2	469.2	469.5	469.9
S-Phase	468.1	468.1	468.3	468.4	–
V-phase (Mg ₂ Zn ₁₁)	461.3	461.3	461.3	–	–
M-phase	–	–	–	–	469.1

Table 7 Mass fraction of the phases at solidus temperatures based on the Scheil solidification simulation of the investigated samples

Phase	Mass fraction of the phase at solidus temperature				
	0	1	2	3	4
Al ₄₅ Cr ₇	0.004	0.004	0.004	0.005	0.004
α _{Al}	0.932	0.927	0.924	0.924	0.938
Al ₁₃ Fe ₄	0.003	0.003	0.003	0.003	0.003
LaSi ₂	–	0.001	0.001	0.002	0.002
Mg ₂ Si	0.002	0.001	0.001	–	–
Al ₇ Cu ₄ Ni	0.001	0.001	0.001	0.001	0.001
Al ₁₁ La ₃	–	–	–	–	0.001
T-Phase	0.036	0.033	0.034	0.035	0.011
S-Phase	0.006	0.005	0.006	0.006	–
V-phase (Mg ₂ Zn ₁₁)	0.006	0.001	0.001	–	–
M-phase	–	–	–	–	0.040
Liquid	Bal.	Bal.	Bal.	Bal.	Bal.

of La affects the liquidus temperature of Mg₂Si, Al₁₈Mg₃Cr, Al₇Cu₂Fe and the T-Phase. However, in the case of Mg₂Si (up to 0.14 mass% La) phase and T-Phase it is obvious that with increasing La addition, the liquidus temperature of the mentioned phases decreases. In the case of Al₁₈Mg₃Cr and

Al₇Cu₂Fe (up to 0.14 mass% La), however, the liquidus temperature also increases with increasing La content.

Table 5 shows the mass fraction of the stable phases at 400 °C for all samples investigated. The main difference with the addition of La is the mass fraction of the S-phase, which increases slightly with the addition of La, and the amount of the T-phase, which decreases with increasing La addition and is no longer present in sample 4. As for the La phases, only the La₂Zn₁₇ phase is stable at 400 °C. According to calculations, La begins to form the La₂Zn₁₇ phase (cyan-coloured curve in Fig. 1) from LaSi₂ (lime-coloured curve in Fig. 1) and Al₁₁La₃ (pink-coloured curve in Fig. 1), which also has the lowest liquidus temperature (Table 4) of all La phases formed in the samples studied.

Since, the as-cast samples were used for microscopic analysis to evaluate phase evolution at a cooling rate of 10 K min⁻¹, Scheil solidification simulations were also performed. In this case, plots showing the mass fractions of the phases during the Scheil solidification simulations (Fig. 2) were prepared for samples 0, 2 and 4. All results concerning the solidus temperatures are shown in Table 6. In addition, we have also listed the mass fraction of the phases in the samples after solidification (Table 7).

Since, the Scheil model simulates solidification, the solidus temperatures are given for the samples studied, as the liquidus temperatures are the same as in the equilibrium calculations. The solidus temperature for sample 0 is 460.3 °C, for sample 1 461.3 °C, for sample 2 461.3 °C, for sample 3 461.3 °C and for sample 4 468.8 °C. The results show that the addition of La does not change the solidification interval significantly (it only changes by 1 °C compared to sample 0). Only sample 4 shows a slightly shorter solidification interval (8.5 °C compared to sample 0).

Based on the Scheil solidification calculations in terms of the liquidus temperatures of the phases (Table 6), the addition of La during solidification forms two new phases (LaSi₂ and Al₁₁La₃—the latter only in sample 4). Compared to the reference sample (0), the addition of La influences the liquidus temperatures of Mg₂Si. The higher the La content, the lower the liquidus temperature of Mg₂Si. For Mg₂Si, the trend is the same as in the equilibrium calculations (Table 4). Another difference is in sample 4, where 0.17 mass% La has an effect on the S-phase and the V-phase, which are no

Table 8 Characteristic temperatures in °C obtained from the DSC cooling curves of all samples investigated

Sample	T _L	Al ₁₃ Fe ₄	Mg ₂ Si/LaSi ₂	α-Al + σ[Mg(Zn, Cu, Al) ₂]	T _S	ΔT (T _L –T _S)
0	635.6	557.9	510.1	470.8	445.2	190.4
1	634.9	556.7	511.9	471.4	443.4	191.5
2	633.9	554.4	522.5	470.7	444.5	189.4
3	632.8	552.3	526.0	470.2	442.5	190.3
4	633.4	553.3	539.5	471.2	444.3	189.1

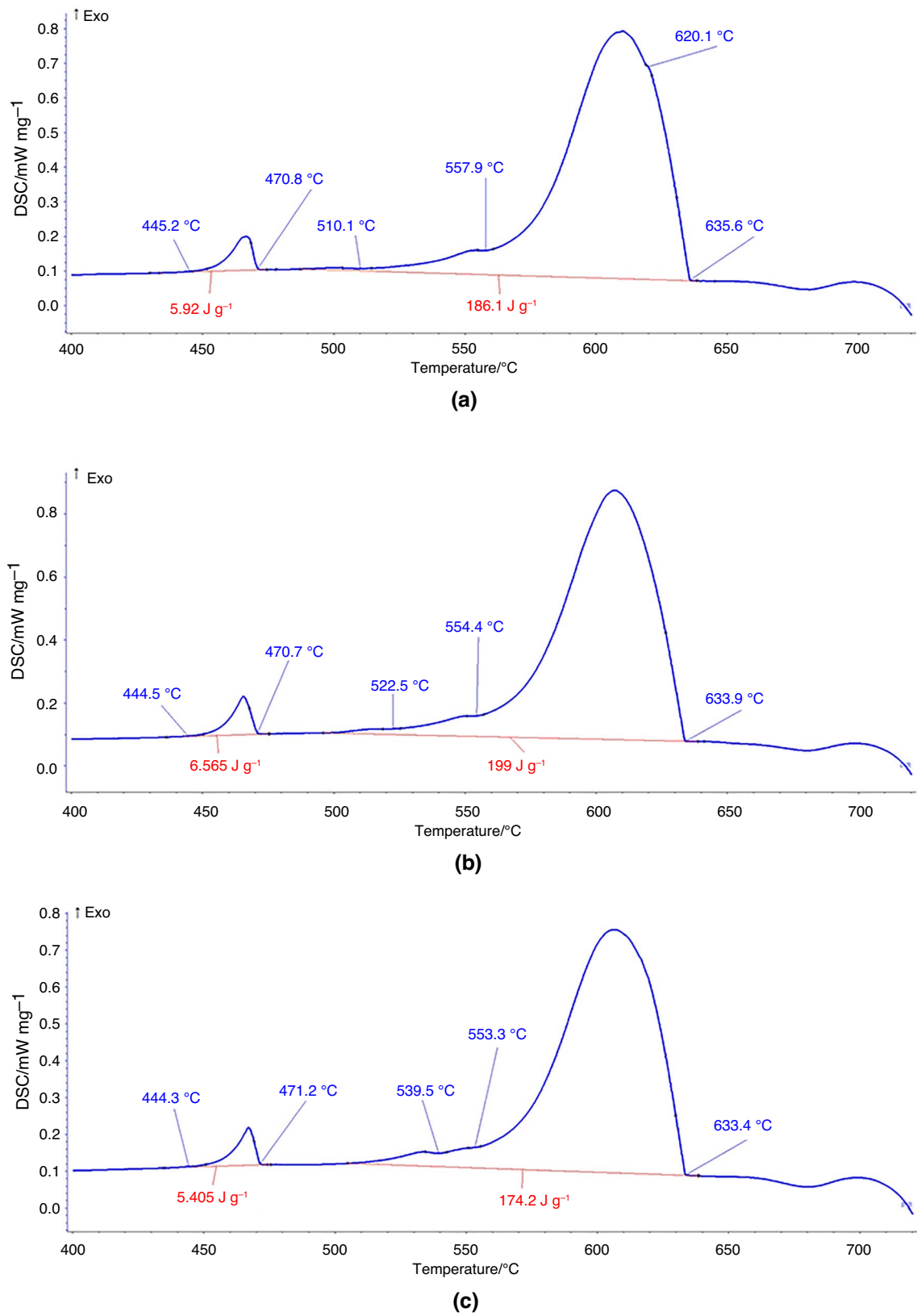


Fig. 3 DSC cooling curves for sample 0 (a), sample 2 (b) and sample 4 (c)

Table 9 Exothermic energies released on cooling of all the samples studied, for the solidification of the matrix and the eutectic $\alpha(\text{Al}) + \sigma[\text{Mg}(\text{Zn}, \text{Cu}, \text{Al})_2]$ phase

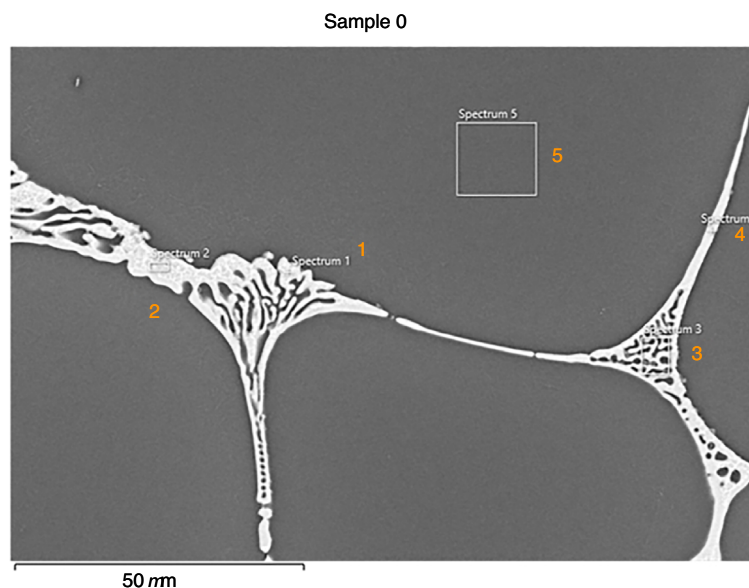
Sample	Solidification enthalpies J g^{-1}	
	Solidification	$\alpha(\text{Al}) + \sigma[\text{Mg}(\text{Zn}, \text{Cu}, \text{Al})_2]$
0	186.1	5.9
1	185.8	5.8
2	199.0	6.6
3	187.7	6.4
4	174.2	5.4

longer present during solidification but form the M-phase. This differs from the equilibrium calculations (Table 4) where the M-phase and the V-phase were not present. The $\text{Al}_7\text{Cu}_2\text{Fe}$, $\text{Al}_{15}\text{Si}_2(\text{Fe}, \text{Cr})_3$ and $\text{Al}_{18}\text{Mg}_3\text{Cr}$ phases are also absent during solidification compared to the results of the equilibrium calculations (Tables 4 and 5). On the other hand, the $\text{Al}_{13}\text{Fe}_4$ phase appears during solidification.

Since, different phases solidify during solidification of the investigated samples based on Scheil calculations compared to equilibrium calculations, a table (Table 7) was also prepared showing the mass fractions of the phases at solidus temperatures of the investigated samples. There is an obvious trend in terms of the amount of La added:

the more La is added to the samples, the less T-phase is present in the samples. It is also clear from the calculations that LaSi_2 is the only La phase present after solidification, except in sample 4 where $\text{Al}_{11}\text{La}_3$ is also present. When we compare the results of the La phases with the results of the equilibrium calculations, in the case of the Scheil solidification simulations, no $\text{La}_2\text{Zn}_{17}$ phase is present after the solidus temperature, which was present in the equilibrium calculations. Moreover, at higher La addition, the S-phase (above 0.14 mass% La) and the V-phase (above 0.10 mass% La) are no longer present during solidification. On the other hand, the M-phase starts to solidify at higher La addition (above 0.14 mass%).

Thus, if we compare the results of two different types of calculations and first consider the La-based phases, it is obvious that after solidification there should be a $\text{La}_2\text{Zn}_{17}$ phase in the samples with La addition, based on equilibrium, but a LaSi_2 phase based on the Scheil solidification calculations. This is confirmed by further analysis (DSC and metallography) to determine which La-based phase is actually present in the samples. The other main difference concerns the T-phase and the S-phase. The results of the equilibrium calculations show that there should be more S-phase in the samples after solidification, but the Scheil calculations show the opposite, that the amount of T-phase should be higher. And the last main difference concerns the Fe-based phase. The results of the equilibrium calculations

Fig. 4 The analysed areas (marked as spectrum in the table) with EDS are with the corresponding chemical composition in at% for sample 0

Chemical element	Spectrum 1	Spectrum 2	Spectrum 3	Spectrum 4	Spectrum 5
Mg	29.73	29.94	15.35	29.36	2.15
Al	30.41	27.35	61.76	32.72	95.23
Cu	20.12	22.05	11.84	18.05	0.31
Zn	19.74	20.66	11.05	19.87	2.28

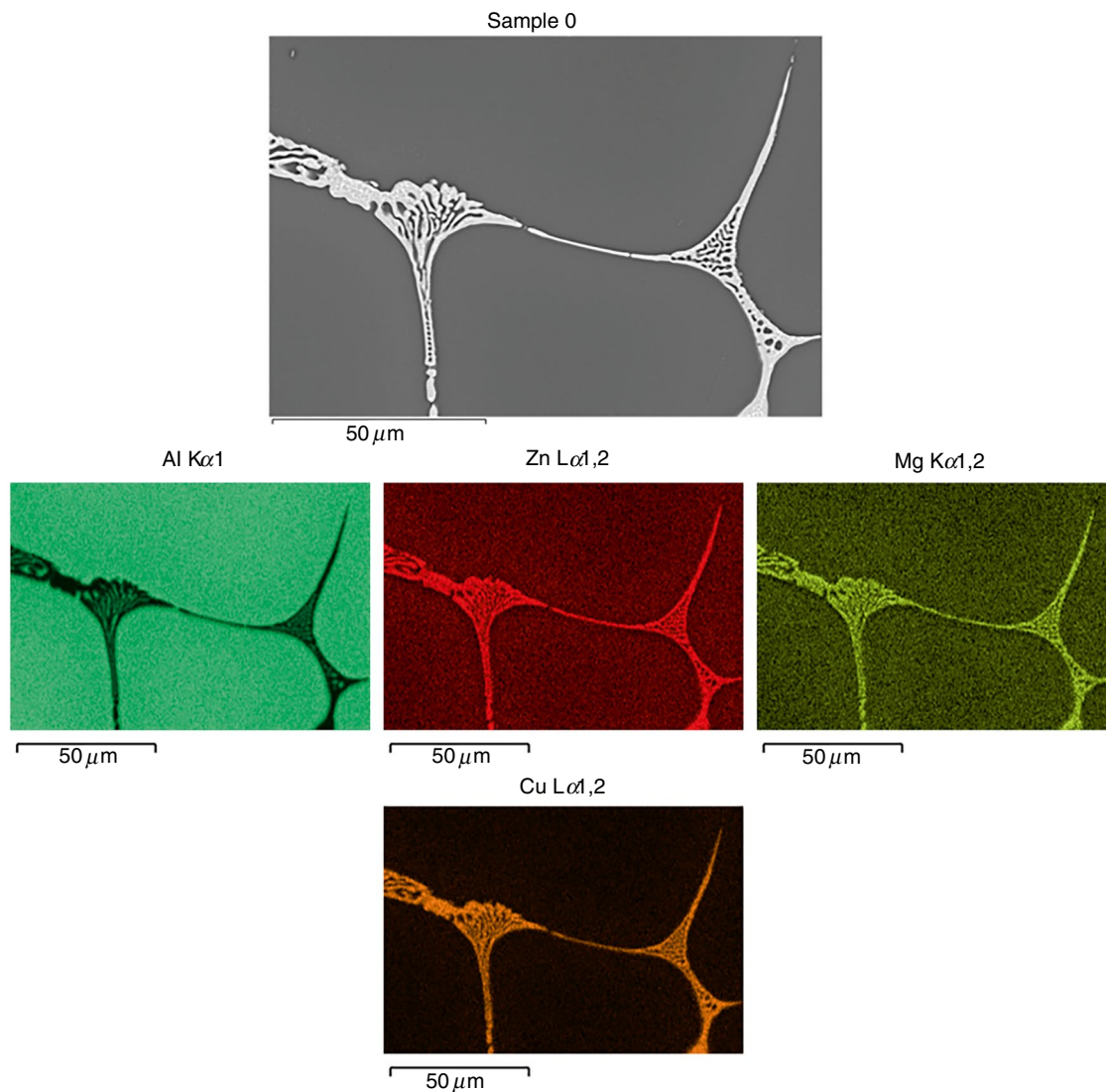


Fig. 5 EDS element mapping images for sample 0

show that the $\text{Al}_7\text{Cu}_2\text{Fe}$ phase should be present, while the Scheil calculations show that the $\text{Al}_{13}\text{Fe}_4$ phase should be present. Since, these phases are well-known and have already been described and characterised by other researchers [1, 2, 5, 7–9, 13, 21], we will only confirm which phases are present in the investigated samples after solidification in the as-cast state by further analysis.

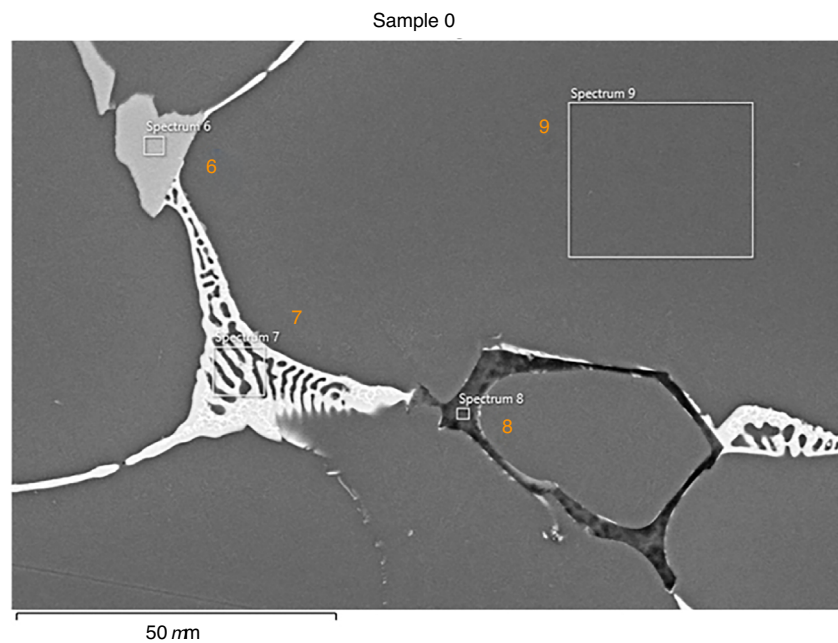
DSC analysis

In the DSC analysis, only the most meaningful diagrams are shown, just as in the CALPHAD calculations, i.e., the DSC cooling curves for samples 0, 2 and 4. However, in the following table (Table 8) we have compiled all the characteristic temperatures obtained from the DSC analysis. In the reference sample (Fig. 3a), an additional peak was determined

at 620.1 °C, which belongs to the liquidus temperature of $\alpha\text{-Al}$ and was no longer visible when La was added.

It is evident from the results that the addition of La does not drastically change the solidification interval (ΔT —Table 8), it remains almost unchanged. However, the addition of La lowers the liquidus temperature of samples 1, 2, 3 and 4 by 0.7, 1.7, 2.8 and 2.2 °C, respectively, compared to the reference sample (0). The results show that the liquidus temperatures decrease up to an addition of 0.14 mass% La and then increase again (sample 4). The same is true for the solidus temperature (1.8, 0.7, 2.7 and 0.9 °C for samples 1, 2, 3 and 4, respectively), but in this case there is no logical trend as the results vary greatly with the addition of La. On the other hand, the liquidus temperature of the $\text{Al}_{13}\text{Fe}_4$ phase starts to decrease with the addition of La (1.2, 3.5, 5.6 and 4.6 °C for samples 1, 2, 3 and 4, respectively). In this case,

Fig. 6 The analysed areas (marked as spectrum in the table) with EDS are indicated with the corresponding chemical composition in at% for sample 0



Chemical element	Spectrum 6	Spectrum 7	Spectrum 8	Spectrum 9
Mg	0.76	13.82	51.49	2.16
Al	75.37	64.77	8.05	95.31
Si	/	/	39.99	/
Mn	0.34	/	/	/
Fe	16.87	/	/	/
Ni	0.40	/	/	/
Cu	5.10	11.33	/	0.38
Zn	1.15	10.08	0.47	2.15

the trend is the same as for the liquidus temperature of the alloy. Moreover, the liquidus temperature increases for the Mg_2Si phase (1.8, 12.4, 15.9 and 29.4 °C for samples 1, 2, 3 and 4 respectively). For the Mg_2Si phase, there is a trend that the liquidus temperature of the Mg_2Si phase increases with increasing La content. The reason for this is that when La is added, a new phase $LaSi_2$ begins to form, which fundamentally changes the Mg_2Si phase. This trend has already been demonstrated in previous studies [42–44]. In sample 2, only a few residues of the Mg_2Si phase are present, the rest being $LaSi_2$ phase, which is confirmed by further microstructural analyses. So, in sample 2, both phases solidify simultaneously. And in the samples with a La addition of more than 0.1 mass%, no Mg_2Si phase was observed in the microstructure in the as-cast state. This means that the liquidus temperature determined in samples 3 and 4 (Table 8) is the liquidus temperature of $LaSi_2$. This is also consistent with the CALPHAD calculations (Tables 4 and 6), which indicate that with the addition of La, the liquidus of the $LaSi_2$ phase begins to increase and the liquidus of the Mg_2Si

phase begins to decrease. Furthermore, the mass fraction of the Mg_2Si phase decreases and the mass fraction of $LaSi_2$ increases with the addition of La (Table 7). In contrast, the liquidus temperature of the eutectic phase ($\alpha-Al + \sigma[Mg(Zn, Cu, Al)_2]$) is not affected. Overall, the addition of La has no influence on the solidification interval, but on the liquidus temperature of the Mg_2Si (and $LaSi_2$ —in samples 3 and 4) and $Al_{13}Fe_4$ phase.

Since, we can also determine the energies released during cooling, we compile them in the following table (Table 9). It is obvious that the addition of La in sample 1 has no influence on the solidification energy. However, in samples 2 and 3, the solidification energy increases, while the addition of 0.17 mass% La decreases the solidification energy. The same trend is observed for the solidification energies of the eutectic $\alpha-Al + \sigma[Mg(Zn, Cu, Al)_2]$ phase. As for the energies, the addition of 0.05 mass% La does not seem to affect them, but 0.1 and 0.14 mass% increase them and 0.17 mass% decrease them.

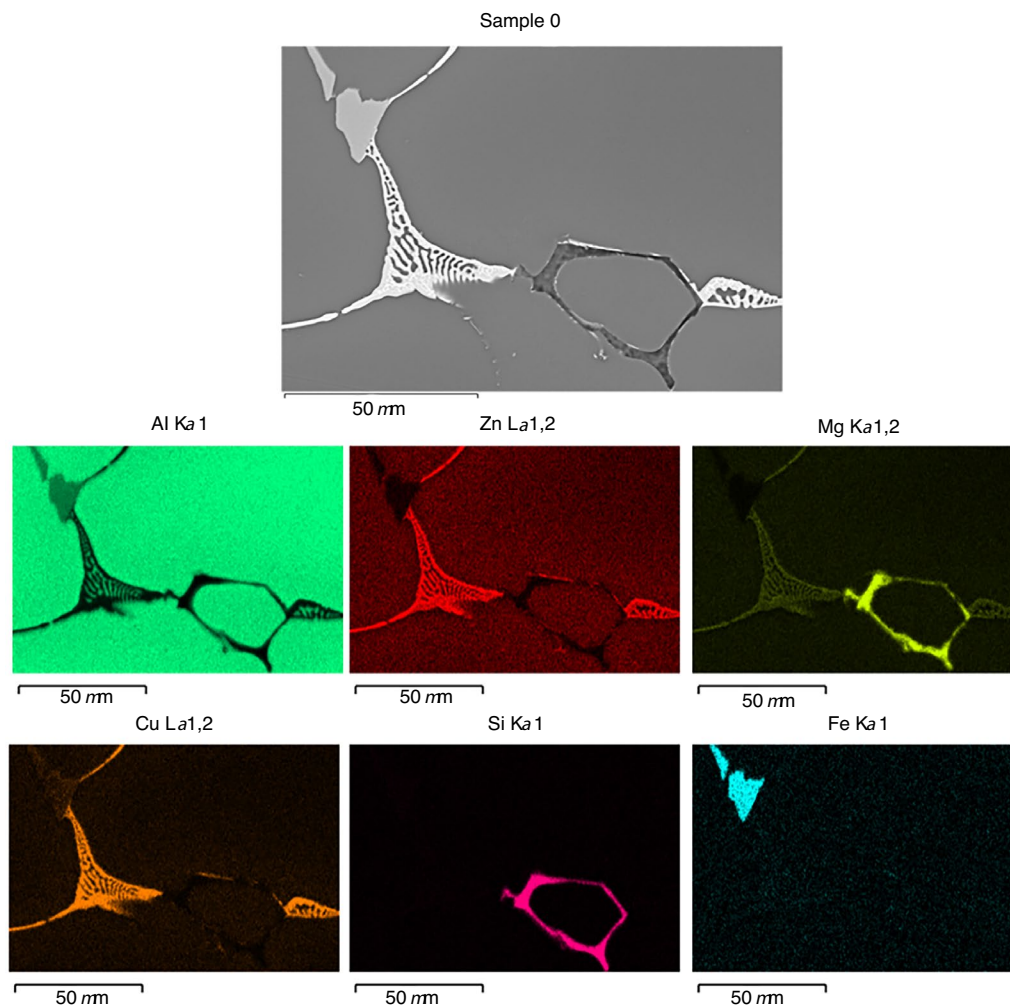


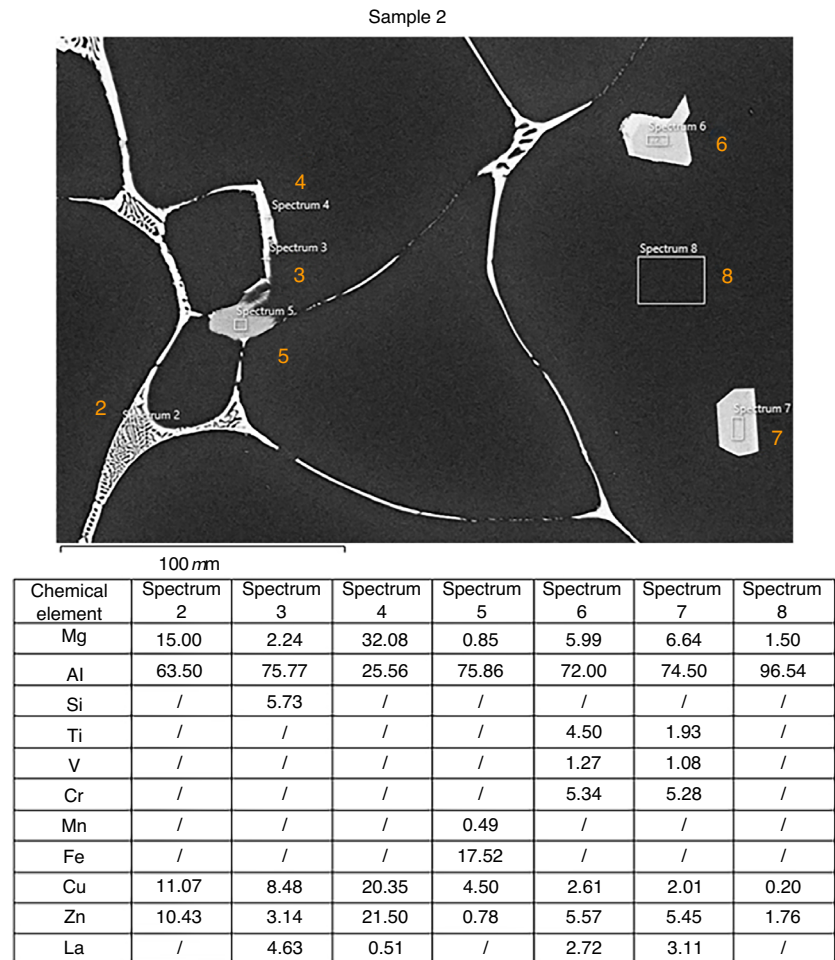
Fig. 7 EDS element mapping images for sample 0

Based on the results of the DSC analysis, we can confirm that the solidus temperatures determined with the Scheil solidification calculations are more accurate than those determined with the equilibrium calculations. But this was somehow to be expected, since the cooling rate during the DSC analysis was 10 K min^{-1} . The liquidus temperatures are lower than the calculated ones, but this was also to be expected due to the undercooling during the DSC analysis. However, from the shape of the peaks of the $\text{Al}_{13}\text{Fe}_4$ and the $\text{Mg}_2\text{Si}/\text{LaSi}_2$ phases, we can see that with the addition of La, the first peak ($\text{Al}_{13}\text{Fe}_4$ phase) slowly becomes flatter, and the second peak ($\text{Mg}_2\text{Si}/\text{LaSi}_2$ phase) slowly becomes more pronounced (Fig. 3). This is related to the solidification of the La-based phase, more specifically the La_2Si phase.

Metallography

Metallographic analysis was carried out to confirm the presence of phases in the microstructure in the as-cast state, as determined by CALPHAD calculations and DSC analyses. For this purpose, an EDS analysis of the phases was present and performed and the results are given in at%. In addition, EDS element mapping was carried out to clarify which phases were present, as the La phases were generally observed above the eutectic phase and the amounts of Zn, Mg and Cu were elevated, as shown. The stoichiometry of the phases differs because they are metastable non-equilibrium phases in the microstructure in the as-cast state. In addition, we also measured the crystal grain size. For sample 0, the average grain size was $114.2 \mu\text{m}$, for sample 2 $116.9 \mu\text{m}$ and for sample 4 $119.3 \mu\text{m}$. The results show that the grain size does not decrease due to the addition of La, but just the opposite. This is probably due to the fact that with the addition of La, a La-based phase ($\text{Al}_{20}\text{Cr}_2\text{La}$) starts

Fig. 8 The analysed areas (marked as spectrum in the table) with EDS are indicated with the corresponding chemical composition in at% for sample 2



to form, the size of which is too large to successfully apply grain refinement as intended (and as is the case with Al_3Ti) when the phase first starts to solidify. This is also consistent with the literature [22–24] where no Cr content was present and the addition of La refined the grains. But unfortunately, the $\text{Al}_{45}\text{Cr}_7$ phase was not found in reference sample 0 because it solidifies first, and the size of the phase is too small to be successfully identified with the SEM analysis.

Figure 4 shows the EDS analysis of sample 0, where the eutectic phase was analysed. Based on the literature [1–10, 12–16, 18–21] and the phase composition in at%, this is the $\alpha(\text{Al}) + \sigma[\text{Mg}(\text{Zn}, \text{Cu}, \text{Al})_2]$ eutectic phase (Fig. 4—Spectrum 3), and we also analysed only the $\sigma[\text{Mg}(\text{Zn}, \text{Cu}, \text{Al})_2]$ phase (Fig. 4—Spectrum 1, 2 and 4). In addition, the matrix was also analysed (Fig. 4—Spectrum 5).

To further confirm that this is indeed a eutectic $\alpha(\text{Al}) + \sigma[\text{Mg}(\text{Zn}, \text{Cu}, \text{Al})_2]$, we also made EDS element mapping images (Fig. 5). It can be seen that there are increased amounts of Mg, Zn and Cu in the phase (in the white areas of the phase) and Al in the darker areas (Fig. 5). This means that it is a eutectic phase, which is

the last to solidify (last peak on the DSC curves during cooling—Fig. 3).

To confirm other phases, present in the microstructure in the as-cast state, we analysed different areas of sample 0 (Fig. 6). Here we can see that the $\text{Al}_{13}\text{Fe}_4$ phase (Spectrum 6—Fig. 6) and the Mg_2Si phase (Spectrum 8—Fig. 6) are present. However, as increased amounts of Zn, Mg and Cu are also present, we have also created EDS element mapping images to confirm these phases (Fig. 7). Meanwhile, we also found the eutectic $\alpha(\text{Al}) + \sigma[\text{Mg}(\text{Zn}, \text{Cu}, \text{Al})_2]$ phase in this area (Spectrum 7—Fig. 6), which we have already analysed (Figs. 4 and 5). An additional EDS analysis of the matrix was performed (Spectrum 9—Fig. 6).

EDS element mapping images of sample 0 (Fig. 7) were made in the same area as in Fig. 6 to confirm that there are three distinct phases: eutectic $\alpha(\text{Al}) + \sigma[\text{Mg}(\text{Zn}, \text{Cu}, \text{Al})_2]$, Mg_2Si and $\text{Al}_{13}\text{Fe}_4$ in the microstructure of reference sample 0 in the as-cast state. To illustrate that it is indeed the $\text{Al}_{13}\text{Fe}_4$ phase (Spectrum 6—Fig. 6), the amounts of Fe and Al are increased at the same location (Fig. 7). The same applies to the Mg_2Si phase (Spectrum 8—Fig. 6), as the amounts of Mg and Si are increased in the same place (Fig. 7).

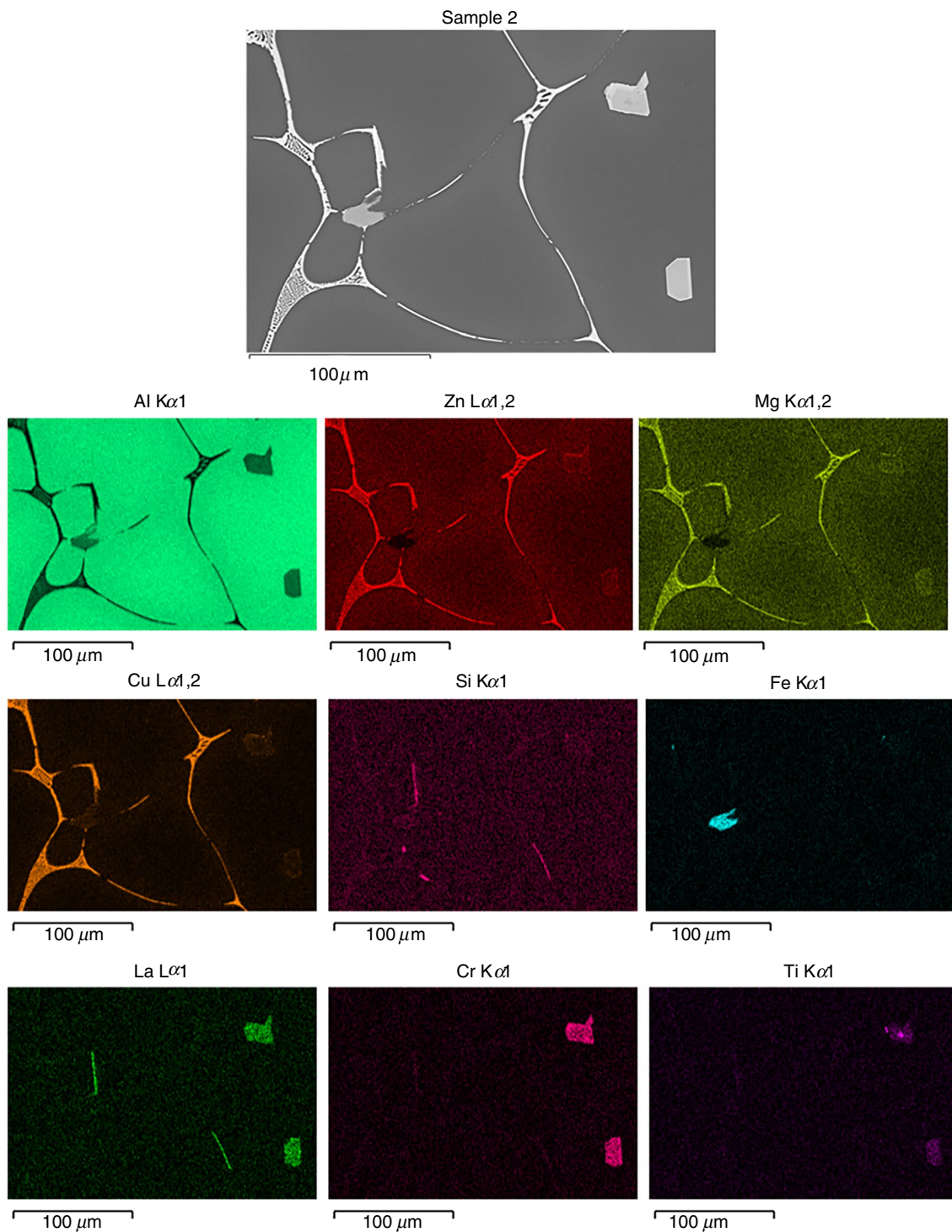
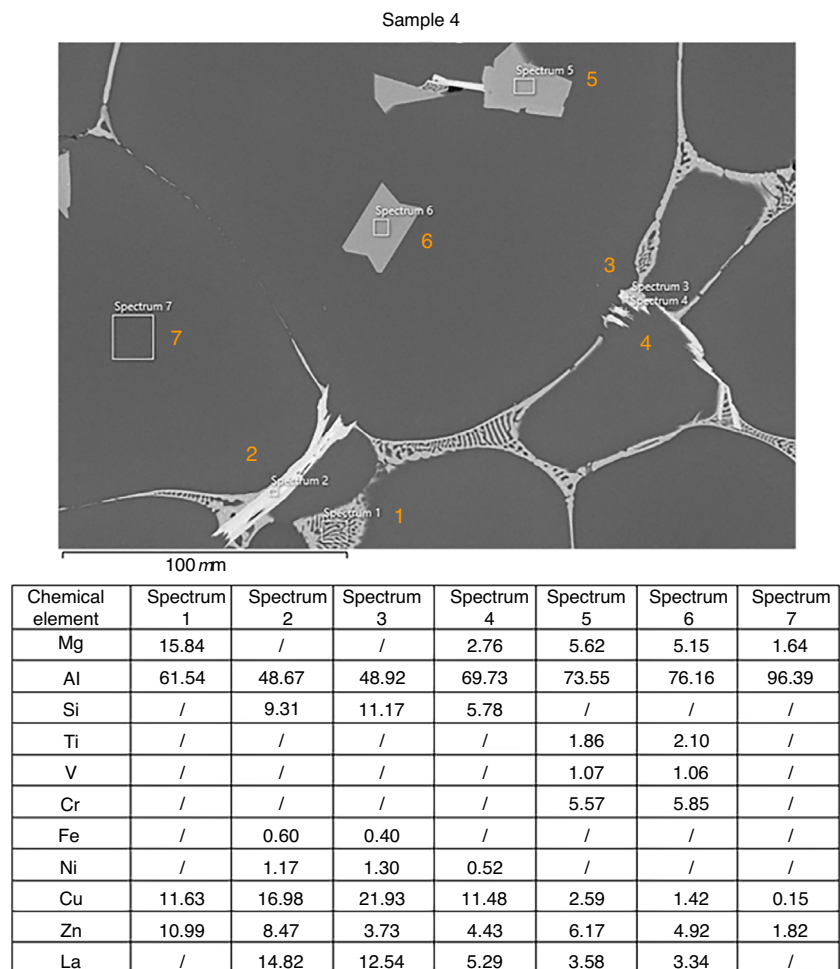


Fig. 9 EDS element mapping images for sample 2

Figure 8 shows the EDS analysis of sample 2, where all phases present in the microstructure in the as-cast state were analysed. Based on the previous results and phase composition Fig. 8—Spectrum 2 and 4 the eutectic phase is $\alpha(\text{Al}) + \sigma[\text{Mg}(\text{Zn}, \text{Cu}, \text{Al})_2]$, but in spectrum 4 there is

a slightly increased La addition, which is further clarified with EDS element mapping images. The next phase is a La-based phase with increased Si content (probably LaSi_2) and the presence of Mg (Fig. 8—Spectrum 3), but as the phase is above the eutectic phase, the content of other elements is

Fig. 10 The analysed areas (marked as spectrum in the table) with EDS are indicated with the corresponding chemical composition in at% for sample 4



also increased. Therefore, additional EDS element mapping was carried out to confirm the LaSi_2 phase with increased Mg content. Another phase present is $\text{Al}_{13}\text{Fe}_4$ (Fig. 8—Spectrum 5). Another new phase besides LaSi_2 appears in the microstructure with the addition of La and this phase is sharp-edged (Fig. 8—Spectrum 6 and 7). This phase has increased amounts of La, Cr and Ti, among other elements present in the matrix (Al, Zn, Mg and Cu). Based on at%, the stoichiometry of this phase cannot be determined, but based on the literature [45, 46] it could be a La-based phase with increased Cr content (probably $\text{Al}_{20}\text{Cr}_2\text{La}$, as no other phase with the combination of these chemical elements is reported in the literature), as, based on CALPHAD calculations (Tables 4 and 6), the $\text{Al}_{45}\text{Cr}_7$ phase starts to solidify first (it seems that it is the nucleus for the growth of the $\text{Al}_{20}\text{Cr}_2\text{La}$ phase), the phase is a sharp-edged phase like $\text{Al}_{45}\text{Cr}_7$ [47–49] and is located in the α -Al crystal grains, which means that it solidifies first. But as mentioned earlier, the $\text{Al}_{45}\text{Cr}_7$ phase was not found in sample 0 because it is too small to be successfully identified by SEM analysis. To confirm this phase and the LaSi_2 phase, we performed an

EDS element mapping (Fig. 9). In addition, the matrix was also analysed (Fig. 8—Spectrum 8).

To confirm that La-based phases are present in the microstructure, Fig. 9 shows the EDS element mapping of the same location as in Fig. 8. The first is LaSi_2 , needle shape phase, as seen in Fig. 9, in which increased amounts of La and Si are present. So basically, Fig. 8—Spectrum 3 is the LaSi_2 phase, but it still contains some amounts of Mg because La is starting to modify the Mg_2Si phase, as mentioned earlier. Another phase based on La is the sharp-edged phase, which according to EDS is probably the $\text{Al}_{20}\text{Cr}_2\text{La}$ phase and has an increased amount of Ti, as shown earlier (Fig. 8—Spectrum 6 and 7). All other phases present are eutectic $\alpha(\text{Al}) + \sigma[\text{Mg}(\text{Zn}, \text{Cu}, \text{Al})_2]$ and $\text{Al}_{13}\text{Fe}_4$.

The microstructure of sample 4 was also examined using the EDS analysis (Fig. 10). In this case, the phases present in the microstructure in the as-cast state are the same as for sample 2. Based on the previous results and the phase composition in at% (Fig. 10), Spectrum 1 is the eutectic phase $\alpha(\text{Al}) + \sigma[\text{Mg}(\text{Zn}, \text{Cu}, \text{Al})_2]$. The next phase present is LaSi_2 with some amounts of Mg (Fig. 10—Spectrum 2, 3 and 4), but as the phase is above the eutectic phase, the amount of

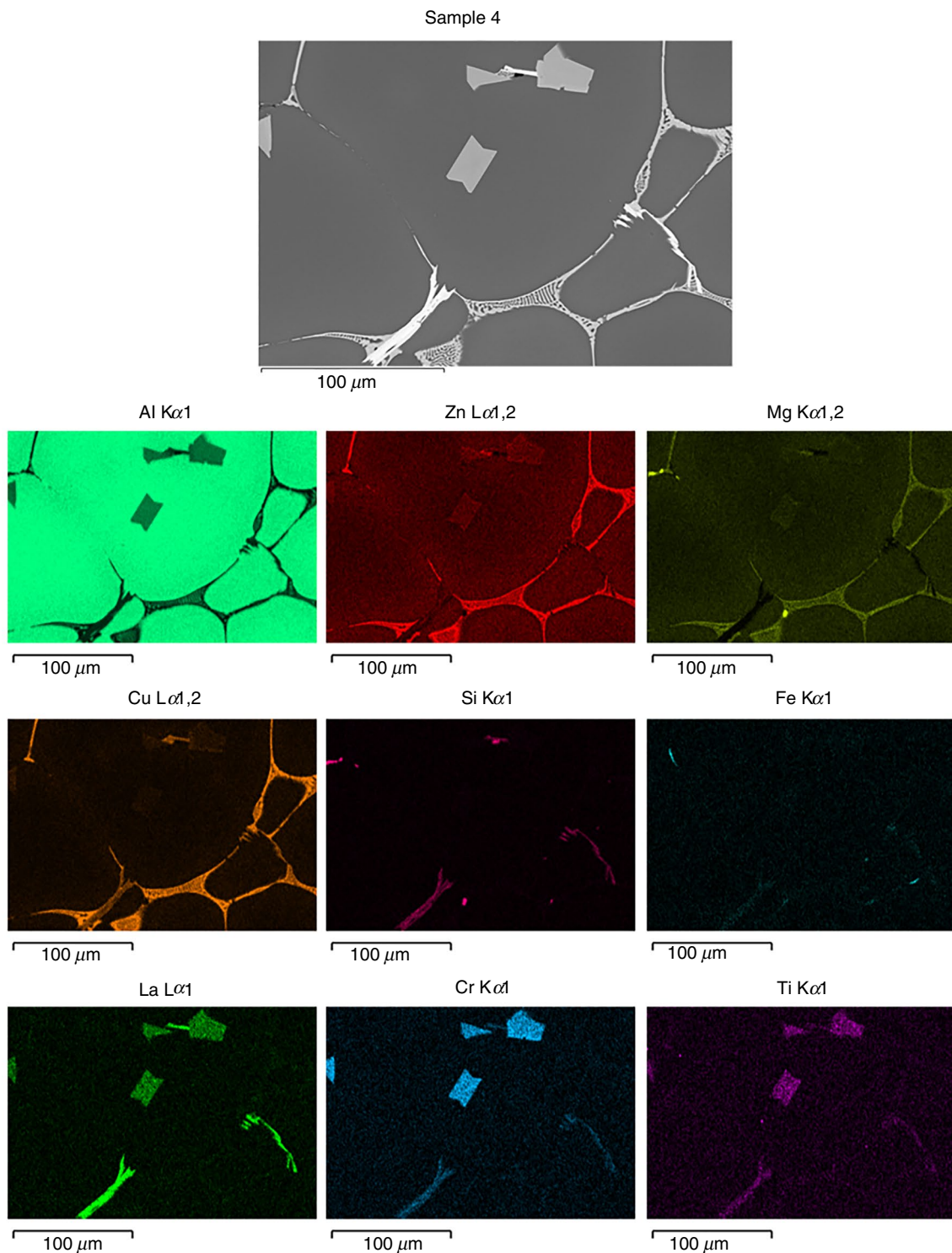


Fig. 11 EDS element mapping images for sample 4

other elements (Al, Zn, Cu, Mg and Ni) was again increased, just as in sample 2. The sharp-edged $\text{Al}_{20}\text{Cr}_2\text{La}$ phase is also present (Fig. 10—Spectrum 5 and 6), again with increased amounts of other elements (Al, Zn, Mg, Cu and V). The matrix was also analysed (Fig. 10—Spectrum 7).

EDS element mapping was also performed for the same area as in Fig. 10 (Fig. 11). The results show that two La-based phases are present in the microstructure. The first is needle-like LaSi_2 . Here, it is clear that the phase shown in Fig. 10—Spectrum 2, 3 and 4—is indeed LaSi_2 , as no Mg

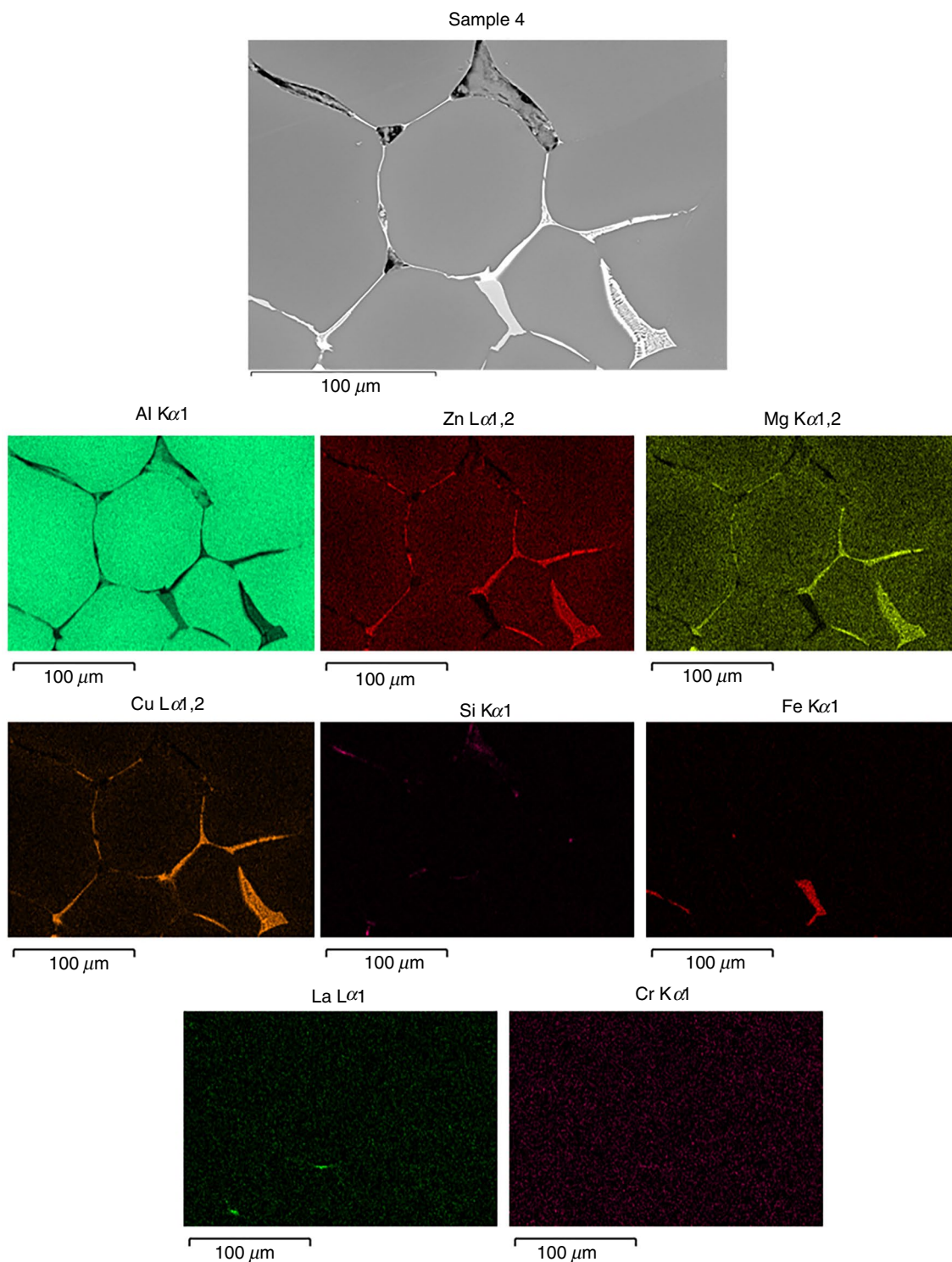


Fig. 12 EDS element mapping images for sample 4

is present and the amounts of La and Si are increased. This also confirms the previous assumptions made when discussing the DSC results. In the samples above 0.1 mass % La, no Mg_2Si phase is present anymore and is completely replaced by the LaSi_2 phase. Furthermore, from the EDS element

mapping, we can confirm that the sharp-edged $\text{Al}_{20}\text{Cr}_2\text{La}$ phase (Fig. 10—Spectrum 5 and 6) is also present, as increased amounts of La and Cr are present. It also appears that higher amounts of Ti are dissolved in this phase, which is also consistent with the assumptions made earlier, as it is

known that Ti is added to Al alloys (as grain refinement— Al_3Ti , etc.) to reduce the size of $\alpha\text{-Al}$ grains as it nucleates prior to solidification of $\alpha\text{-Al}$. This means that this phase ($\text{Al}_{20}\text{Cr}_2\text{La}$) starts to solidify first and based on the CALPHAD calculations, the first phase to solidify is $\text{Al}_{45}\text{Cr}_7$. So, this means that the addition of La not only changes the Mg_2Si phase, but also the Cr-based phase mentioned earlier. No $\text{Al}_{13}\text{Fe}_4$ phase was found in this region. To confirm these results, we performed another EDS element mapping analysis (Fig. 12) to show that the mentioned phase is still present in the microstructure.

As mentioned earlier, Fig. 12 EDS element mapping images were taken only to confirm that the $\text{Al}_{13}\text{Fe}_4$ phase is still present in the microstructure of sample 4, as it was not present in Figs. 10 and 11. From the following results (Fig. 12), we can see that the $\text{Al}_{13}\text{Fe}_4$ phase is still present, while increased amounts of Fe and Al are present in the same phase. Here we also see the eutectic $\alpha(\text{Al}) + \sigma[\text{Mg}(\text{Zn}, \text{Cu}, \text{Al})_2]$ phase and some tiny needles of the LaSi_2 phase. In sample 4, on the other hand, there was no Mg_2Si phase.

To clarify the observation regarding the La phases: This is only a first insight into the phase stoichiometry of the La-based phases and needs to be further investigated with TEM and XRD analyses, but the phase stoichiometry is not crucial for the effects on solidification.

Conclusions

As far as solidification is concerned, the CALPHAD results show that the addition of La has minimal effect on the liquidus temperature. The solidus temperature increases slightly in the equilibrium calculations, while the solidification interval decreases slightly compared to the reference sample 0, although no significant differences are observed.

Similarly, the Scheil simulations show increased solidus temperatures, with smaller differences for the first three samples compared to the equilibrium temperatures. The addition of La does not significantly change the solidification, apart from a slight shrinkage of the solidification interval in sample 4.

In comparing the phases, we have noted some differences between the two types of calculations. Concerning the La-based phases, the equilibrium calculations predict the presence of a $\text{La}_2\text{Zn}_{17}$ phase after solidification in samples with La addition, while the Scheil solidification calculations suggest a LaSi_2 phase. Another notable difference concerns the T-phase and the S-phase. Equilibrium calculations suggest a higher presence of S-phase after solidification, while Scheil calculations suggest a higher amount of T-phase. Finally, there is a discrepancy in the Fe-based phase. Equilibrium calculations predict the presence of the $\text{Al}_7\text{Cu}_2\text{Fe}$

phase, while Scheil calculations suggest the presence of the $\text{Al}_{13}\text{Fe}_4$ phase.

The DSC results support the CALPHAD calculations and show that the addition of La does not drastically affect the liquidus and solidus temperatures. However, the addition of La lowers the liquidus temperature. The solidus temperatures also decrease with the addition of La, but the results show that there is no logical trend. The solidification interval remains largely unchanged. The liquidus temperature of the $\text{Al}_{13}\text{Fe}_4$ phase decreases with the addition of La, while the liquidus temperature of the Mg_2Si phase increases. This is due to the formation of a new phase, LaSi_2 , which fundamentally changes the Mg_2Si phase. In sample 2, only remnants of the Mg_2Si phase are present, while the majority consists of the LaSi_2 phase. Samples with more than 0.1 mass% of La do not show any Mg_2Si phase in the microstructure in the as-cast state. The addition of La has no effect on the liquidus temperature of the eutectic phase ($\alpha\text{-Al} + \sigma[\text{Mg}(\text{Zn}, \text{Cu}, \text{Al})_2]$). Another La-based phase, $\text{Al}_{20}\text{Cr}_2\text{La}$, starts to form with the addition of La. It modifies the $\text{Al}_{45}\text{Cr}_7$ phase and solidifies first. Interestingly, the grain size does not decrease with the addition of La, but rather increases. This is probably because the formation of the La-based phase ($\text{Al}_{20}\text{Cr}_2\text{La}$) occurs earlier, and its size is too large for effective grain refinement as intended.

Author contributions All authors contributed to the conception and design of the study. Preparation of materials, conducting the experiments, data collection and analysis were carried out by Tilen Balaško, Maja Vončina, Jožef Medved and Aleš Nagode. The first draft of the manuscript was written by Tilen Balaško and all authors commented on earlier versions of the manuscript. All authors read and approved the final manuscript.

Declarations

Conflict of interest The authors declare that they have no conflict of interest.

Open Access This article is licensed under a Creative Commons Attribution 4.0 International License, which permits use, sharing, adaptation, distribution and reproduction in any medium or format, as long as you give appropriate credit to the original author(s) and the source, provide a link to the Creative Commons licence, and indicate if changes were made. The images or other third party material in this article are included in the article's Creative Commons licence, unless indicated otherwise in a credit line to the material. If material is not included in the article's Creative Commons licence and your intended use is not permitted by statutory regulation or exceeds the permitted use, you will need to obtain permission directly from the copyright holder. To view a copy of this licence, visit <http://creativecommons.org/licenses/by/4.0/>.

References

- Huang R, Li M, Yang H, Lu S, Zuo H, Zheng S, et al. Effects of Mg contents on microstructures and second phases of as-cast Al–Zn–Mg–Cu alloys. *J Mater Res Technol*. 2022;21:2105–17. <https://doi.org/10.1016/j.jmrt.2022.10.050>.
- Jia P, Cao Y, Geng Y, He L, Xiao N, Cui J. Studies on the microstructures and properties in phase transformation of homogenized 7050 alloy. *Mater Sci Eng A*. 2014;612:335–42. <https://doi.org/10.1016/j.msea.2014.06.027>.
- Priya P, Johnson DR, Krane MJM. Precipitation during cooling of 7XXX aluminum alloys. *Comput Mater Sci*. 2017;139:273–84. <https://doi.org/10.1016/j.commatsci.2017.08.008>.
- Liu TW, Wang QD, Tang HP, Li ZY, Lei C, Ebrahimi M, et al. Microstructure and mechanical properties of squeeze-cast Al–5.0Mg–3.0Zn–1.0Cu alloys in solution-treated and aged conditions. *Trans Nonferrous Met Soc China*. 2020;30:2326–38. [https://doi.org/10.1016/S1003-6326\(20\)65382-1](https://doi.org/10.1016/S1003-6326(20)65382-1).
- Rometsch PA, Zhang Y, Knight S. Heat treatment of 7xxx series aluminium alloys—some recent developments. *Trans Nonferrous Met Soc China*. 2014;24:2003–17. [https://doi.org/10.1016/S1003-6326\(14\)63306-9](https://doi.org/10.1016/S1003-6326(14)63306-9).
- Liu J, Hu R, Zheng J, Zhang Y, Ding Z, Liu W, et al. Formation of solute nanostructures in an Al–Zn–Mg alloy during long-term natural aging. *J Alloys Compd*. 2020;821: 153572. <https://doi.org/10.1016/j.jallcom.2019.153572>.
- Zhang Y, Milkereit B, Kessler O, Schick C, Rometsch PA. Development of continuous cooling precipitation diagrams for aluminium alloys AA7150 and AA7020. *J Alloys Compd*. 2014;584:581–9. <https://doi.org/10.1016/j.jallcom.2013.09.014>.
- Lim ST, Eun IS, Nam SW. Control of equilibrium phases (M, T, S) in the modified aluminum alloy 7175 for thick forging applications. *Mater Trans*. 2003;44:181–7. <https://doi.org/10.2320/matertrans.44.181>.
- Ghiaasiaan R, Zeng X, Shankar S. Controlled diffusion solidification (CDS) of Al–Zn–Mg–Cu (7050): microstructure, heat treatment and mechanical properties. *Mater Sci Eng A*. 2014;594:260–77. <https://doi.org/10.1016/j.msea.2013.11.087>.
- Subroto T, Eskin DG, Miroux A, Ellingsen K, M'Hamdi M, Katgerman L. Semi-solid constitutive parameters and failure behavior of a cast AA7050 alloy. *Metall Mater Trans A*. 2021;52:871–88. <https://doi.org/10.1007/s11661-020-06112-5>.
- Williams JC, Starke EA. Progress in structural materials for aerospace systems. *Acta Mater*. 2003;51:5775–99. <https://doi.org/10.1016/j.actamat.2003.08.023>.
- Yuan DL, Chen SY, Chen KH, Huang LP, Chang JY, Zhou L, et al. Correlations among stress corrosion cracking, grain-boundary microchemistry, and Zn content in high Zn-containing Al–Zn–Mg–Cu alloys. *Trans Nonferrous Met Soc China*. 2021;31:2220–31. [https://doi.org/10.1016/S1003-6326\(21\)65650-9](https://doi.org/10.1016/S1003-6326(21)65650-9).
- He KZ, Tan ZM, Zheng X, Zhang XM, Zhou KC. Microstructure and mechanical properties of DC cast 7065 aluminum alloy. *J Phys Conf Ser*. 2021. <https://doi.org/10.1088/1742-6596/1906/1/012051>.
- Masterson C, Jolliffe R. Strengthening of 7175 Aluminum Alloy Through Multi-Step Aging Process. 2021;26. Available from: <https://digitalcommons.calpoly.edu/cgi/viewcontent.cgi?article=1250&context=matesp>
- Österreicher JA, Kirov G, Gerstl SSA, Mukeli E, Grabner F, Kumar M. Stabilization of 7xxx aluminium alloys. *J Alloys Compd*. 2018;740:167–73. <https://doi.org/10.1016/j.jallcom.2018.01.003>.
- Hou S, Zhang D, Ding Q, Zhang J, Zhuang L. Solute clustering and precipitation of Al–5.1Mg–0.15Cu–xZn alloy. *Mater Sci Eng A*. 2019;759:465–78. <https://doi.org/10.1016/j.msea.2019.05.066>.
- Suh DW, Lee SY, Lee KH, Lim SK, Oh KH. Microstructural evolution of Al–Zn–Mg–Cu–(Sc) alloy during hot extrusion and heat treatments. *J Mater Process Technol*. 2004;155–156:1330–6. <https://doi.org/10.1016/j.jmatprotec.2004.04.195>.
- Wolverton C. Crystal structure and stability of complex precipitate phases in Al–Cu–Mg–(Si) and Al–Zn–Mg alloys. *Acta Mater*. 2001;49:3129–42. [https://doi.org/10.1016/S1359-6454\(01\)00229-4](https://doi.org/10.1016/S1359-6454(01)00229-4).
- Li C, Chen Z, Zeng S, Cheng N, Chen T. Intermetallic phase formation and evolution during homogenization and solution in Al–Zn–Mg–Cu alloys. *Sci China Technol Sci*. 2013;56:2827–38. <https://doi.org/10.1007/s11431-013-5356-5>.
- Gao F, Zhao G, Bian W, Tian N. TEM in-situ investigation on non-equilibrium eutectics in semicontinuous casting ingot of Al–6.2Zn–2.3Mg–2.3Cu super-high strength aluminum alloy. *Mater Sci Forum*. 2010;638–642:384–9. <https://doi.org/10.4028/www.scientific.net/MSF.638-642.384>.
- Fan X, Jiang D, Meng Q, Zhong L. The microstructural evolution of an Al–Zn–Mg–Cu alloy during homogenization. *Mater Lett*. 2006;60:1475–9. <https://doi.org/10.1016/j.matlet.2005.11.049>.
- Jiang H, Li S, Zhang L, He J, Zheng Q, Song Y, et al. The influence of rare earth element lanthanum on the microstructures and properties of as-cast 8176 (Al–0.5Fe) aluminum alloy. *J Alloys Compd*. 2021;859:157804. <https://doi.org/10.1016/j.jallcom.2020.157804>.
- Yuan WH, An BL. Effect of La addition on the microstructures and mechanical properties of 7075 aluminum alloy. *Adv Mater Res*. 2010;152–153:1810–3. <https://doi.org/10.4028/www.scientific.net/AMR.152-153.1810>.
- Xu Y, Peng Z, Ding D, Zhang W, Gao Y, Chen G, et al. Effect of La addition on microstructure and properties of Al–0.2Fe–0.06Cu alloy. *Metals*. 2022. <https://doi.org/10.3390/met12020211>.
- Hosseinifar M, Malakhov DV. Effect of Ce and La on microstructure and properties of a 6xxx series type aluminum alloy. *J Mater Sci*. 2008;43:7157–64. <https://doi.org/10.1007/s10853-008-3022-2>.
- Li Q, Xia T, Lan Y, Zhao W, Fan L, Li P. Effect of rare earth cerium addition on the microstructure and tensile properties of hypereutectic Al–20%Si alloy. *J Alloys Compd*. 2013;562:25–32. <https://doi.org/10.1016/j.jallcom.2013.02.016>.
- Medvedev AE, Murashkin MY, Enikeev NA, Valiev RZ, Hodgson PD, Lapovok R. Enhancement of mechanical and electrical properties of Al–RE alloys by optimizing rare-earth concentration and thermo-mechanical treatment. *J Alloys Compd*. 2018;745:696–704. <https://doi.org/10.1016/j.jallcom.2018.02.247>.
- Pérez-Bustamante R, Reyna-Cruz A, Acosta-Peña DC, Santillán-Rodríguez CR, Matutes-Aquino JA, Pérez-Bustamante F, et al. Effect of cerium/lanthanum addition on microstructure and mechanical properties of Al7075 alloy via mechanical alloying and sintering. *J Rare Earths*. 2016;34:420–7. [https://doi.org/10.1016/S1002-0721\(16\)60043-1](https://doi.org/10.1016/S1002-0721(16)60043-1).
- Tang P, Li W, Zhao Y, Wang K, Li W, Zhan F. Influence of strontium and lanthanum simultaneous addition on microstructure and mechanical properties of the secondary Al–Si–Cu–Fe alloy. *J Rare Earths*. 2017;35:485–93. [https://doi.org/10.1016/S1002-0721\(17\)60938-4](https://doi.org/10.1016/S1002-0721(17)60938-4).
- La Torre EA, De P-B, Camarillo-Cisneros J, Gómez-Esparza CD, Medrano-Prieto HM, Martínez-Sánchez R. Mechanical properties of the A356 aluminum alloy modified with La/Ce. *J Rare Earths*. 2013;31:811–6. [https://doi.org/10.1016/S1002-0721\(12\)60363-9](https://doi.org/10.1016/S1002-0721(12)60363-9).
- Gulliver GH. The quantitative effect of rapid cooling upon the constitution of binary alloys. *J Inst Met*. 1913;9:120–57.

32. Scheil E. Bemerkungen zur schichtkristallbildung. *Zeitschrift für Metallkunde. Int J Mater Res.* 1942;34:70–2. <https://doi.org/10.1515/ijmr-1942-340303>.
33. Keller T, Lindwall G, Ghosh S, Ma L, Lane BM, Zhang F, et al. Application of finite element, phase-field, and CALPHAD-based methods to additive manufacturing of Ni-based superalloys. *Acta Mater.* 2017;139:244–53. <https://doi.org/10.1016/j.actamat.2017.05.003>.
34. Schmid-Fetzer R, Kozlov A. Thermodynamic aspects of grain growth restriction in multicomponent alloy solidification. *Acta Mater.* 2011;59:6133–44. <https://doi.org/10.1016/j.actamat.2011.06.026>.
35. Luo AA. Material design and development: from classical thermodynamics to CALPHAD and ICME approaches. *Calphad.* 2015;50:6–22. <https://doi.org/10.1016/j.calphad.2015.04.002>.
36. Eiken J, Subasic E, Lacaze J. 3D phase-field computations of microsegregation in nodular cast iron compared to experimental data and Calphad-based Scheil-prediction. *Materialia.* 2020;9:100538. <https://doi.org/10.1016/j.mtla.2019.100538>.
37. Schaffnit P, Stallybrass C, Konrad J, Stein F, Weinberg M. A Scheil-Gulliver model dedicated to the solidification of steel. *Calphad.* 2015;48:184–8. <https://doi.org/10.1016/j.calphad.2015.01.002>.
38. Smetana B, Žaludová M, Zlá S, Dobrovská J, Cagala M, Szurman I, et al. Application of high temperature DTA technique to Fe based systems. In: *Metals 2010—19th International Conference on Metallurgy and Materials Conference Proceedings 2010*; 357–62.
39. Wielgosz E, Kargul T. Differential scanning calorimetry study of peritectic steel grades. *J Therm Anal Calorim.* 2015;119:1547–53. <https://doi.org/10.1007/s10973-014-4302-5>.
40. Perricone MJ, Dupont JN. Effect of composition on the solidification behavior of several Ni–Cr–Mo and Fe–Ni–Cr–Mo alloys. *Metall Mater Trans A.* 2006;37:1267–80. <https://doi.org/10.1007/s11661-006-1078-7>.
41. Balaško T, Burja J, Medved J. Effect of Ni on solidification of duplex low-density steels. *J Therm Anal Calorim.* 2020;142:1605–11. <https://doi.org/10.1007/s10973-020-10254-4>.
42. Akhlaghi A, Noghani M, Emamy M. The effect of La-intermetallic compounds on tensile properties of Al-15%Mg₂Si in-situ composite. *Procedia Mater Sci.* 2015;11:55–60. <https://doi.org/10.1016/j.mspro.2015.11.085>.
43. Deev V, Prusov E, Shurkin P, Ri E, Smetanyuk S, Chen X, et al. Effect of La addition on solidification behavior and phase composition of cast Al–Mg–Si alloy. *Metals.* 2020;10:1–12. <https://doi.org/10.3390/met10121673>.
44. Wang L, Guo E, Ma B. Modification effect of lanthanum on primary phase Mg₂Si in Mg–Si alloys. *J Rare Earths.* 2008;26:105–9. [https://doi.org/10.1016/S1002-0721\(08\)60047-2](https://doi.org/10.1016/S1002-0721(08)60047-2).
45. Kangas MJ, Schmitt DC, Sakai A, Nakatsuji S, Chan JY. Structure and physical properties of single crystal PrCr₂Al₂₀ and CeM₂Al₂₀ (M = V, Cr): a comparison of compounds adopting the CeCr₂Al₂₀ structure type. *J Solid State Chem.* 2012;196:274–81. <https://doi.org/10.1016/j.jssc.2012.06.035>.
46. Treadwell LJ, McAlpin JD, Schmitt DC, Kangas MJ, Sougrati MT, Haldolaarachchige N, et al. Investigation of Fe incorporation in LnCr₂Al₂₀ (Ln = La, Gd, Yb) with ⁵⁷Fe Mössbauer and single crystal X-ray diffraction. *Inorg Chem.* 2013;52:5055–62. <https://doi.org/10.1021/ic302805n>.
47. Cui Y, Gourlay CM. Growth twinning and morphology of Al₄₅Cr₇ and Al₁₃Fe₄. *J Alloys Compd.* 2022;893:162318. <https://doi.org/10.1016/j.jallcom.2021.162318>.
48. Zhou Z, Li Z, Xie Y, Wang X, Liu Y, Long Z, et al. Experimental study of the phase relationships in the Al-rich corner of the Al–Si–Fe–Cr quaternary system at 700 °C. *Int J Mater Res.* 2015;106:470–80. <https://doi.org/10.3139/146.111202>.
49. Boulet P, De Weerd MC, Gaudry E, Ledieu J, Fournée V. Single crystal growth, crystal structure and surface characterisation of the binary phase Al₄₅Cr₇. *J Phys Conf Ser.* 2020. <https://doi.org/10.1088/1742-6596/1458/1/012016>.

Publisher's Note Springer Nature remains neutral with regard to jurisdictional claims in published maps and institutional affiliations.